Electronic properties of structural twin and antiphase boundaries in materials with strong electron-lattice couplings

K. H. Ahn,* T. Lookman, A. Saxena, and A. R. Bishop
Theoretical Division, Los Alamos National Laboratory, Los Alamos, New Mexico 87545, USA
(Received 2 August 2004; revised manuscript received 31 January 2005; published 10 June 2005)

Using a symmetry-based atomic scale theory of lattice distortions, we demonstrate that elastic textures, such as twin and antiphase boundaries, can generate intricate electronic heterogeneities in materials with strong electron-lattice coupling, as observed in perovskite manganites and other functional electronic materials.

DOI: 10.1103/PhysRevB.71.212102 PACS number(s): 73.20.−r, 61.72.−y, 68.35.−p, 74.81.−g

Recent advances in imaging techniques have revealed the presence of rich elastic textures in functional materials such as colossal magnetoresistive (CMR) manganites,[1,2] ferroelectrics,[3] ferroelastics,[4] and shape memory alloys.[5] In particular, experiments on certain perovskite manganite compounds[2] have shown the correlation between electronic transport properties and the presence of meandering antiphase boundaries (APBs) within insulating charge ordered domains, interpreted as the existence of metallic regions forming around APBs. It is also reported that strains near grain boundaries in thin film can significantly modify electronic properties in manganites.[6] The interplay between elastic texture and electronic heterogeneity is thus central to understanding multiphase coexistence and resultant electronic properties in CMR and other functional electronic materials.

In this work we illustrate the importance of elastic heterogeneities in modifying electronic properties in materials with strong electron-lattice coupling. In particular, we study the electronic properties of APBs and twin boundaries (TBs) on a two-dimensional (2D) lattice. We first show how our recently developed symmetry-based atomic-scale theory of lattice distortions can be used to find atomic configurations of twin and antiphase boundaries. Within our framework, we illustrate the differences and similarities between TBs and APBs from the point of view of localization of long (short) wavelength modes inside APBs (TBs), evolution upon energy relaxation and roughness[7] (smoothness) of APBs (TBs). We subsequently perform a tight binding calculation with a Su-Schrieffer-Heeger (SSH) type model of electron-lattice coupling to predict the distribution of electronic density of states, which can be related to the results of scanning tunneling microscope (STM) measurements. Our work thus forms the basis for predicting electronic properties from predesigned materials microstructures.

Twin boundaries separate domains related by the rotation of crystalline axes, whereas APBs represent boundaries at which the sequence of alternating distortions, such as alternating rotational directions of oxygen octahedra in perovskite oxides, change their phase (i.e., broken translational symmetry). Although our method can be applied to 2D or 3D lattices with monatomic or multiatomic bases, we illustrate our ideas with a square lattice in 2D space (planar *P*4*mm*) with a monatomic basis, for which the appropriate atomic scale distortion variables are the modes shown in Fig. 1. These modes have important advantages over displacement variables—they reflect the symmetries of the lattice and can serve as order parameters (OPs) in structural phase transitions.[8] Therefore, energy expressions with desired ground states can be written in a simpler way in these variables than in usual displacement variables. Moreover, since the lattice distortions are decomposed into the modes at $\vec{k}=(0,0)$ (long-wavelength or intercell modes) and $\vec{k}=(\pi,\pi)$ (short-wavelength or intracell modes), the approach using these modes reveals the differences between long and short wavelength lattice distortions in a natural way.

We consider APBs, such as the one shown in Fig. 2 where open circles represent the distorted atomic positions, for s_x or s_y modes.[9] The simplest energy expression yielding a ground state with either pure s_x or s_y mode lattice distortion is

$$E_{sxsy}=\sum_{\vec{i}}\left\{-\frac{D}{2}[s_x(\vec{i})^2+s_y(\vec{i})^2]+\frac{G_1}{4}[s_x(\vec{i})^4+s_y(\vec{i})^4]+\frac{G_2}{2}s_x(\vec{i})^2s_y(\vec{i})^2\right\}+\sum_{\vec{i},n=1,2,3}\frac{C_n}{2}e_n(\vec{i})^2, \quad (1)$$

where the coefficients D, G_1, G_2 (with $G_1<G_2$) can be obtained from interatomic forces and C_n are the associated elastic moduli.

Since the ground state has $\vec{k}=(\pi,\pi)$ component lattice distortions, we define variables with tilde by multiplying $(-1)^{i_x+i_y}$ with all intercell/intracell/displacement variables [e.g., $\tilde{s}_x(\vec{i})=s_x(\vec{i})(-1)^{i_x+i_y}$, $\tilde{d}_x(\vec{i})=d_x(\vec{i})(-1)^{i_x+i_y}$]. In wave vector space, this corresponds to interchanging the (0,0) and (π,π) points. Therefore, $\tilde{s}_x$ and $\tilde{s}_y$ are the modes near $\vec{q}=(0,0)$, and $\tilde{e}_1$, $\tilde{e}_2$, and $\tilde{e}_3$ are the modes near $\vec{q}=(\pi,\pi)$, where $\vec{q}$ represents the wave vector for the variables with tilde. The constraint equations in the continuum limit are $\tilde{e}_{1,3}(\vec{r})=(\nabla_y\tilde{s}_x\pm\nabla_x\tilde{s}_y)/(2\sqrt{2})$ and $\tilde{e}_2(\vec{r})=(\nabla_x\tilde{s}_x+\nabla_y\tilde{s}_y)/(2\sqrt{2})$. These relations show that spatial variations of *intracell*

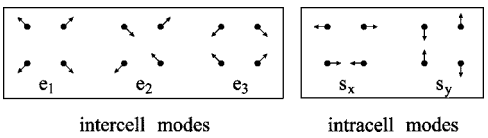

FIG. 1. Distortion modes for a 2D square lattice with a monatomic basis, for example, $s_x(\vec{i})=\{d^x(\vec{i})-d^x[\vec{i}+(10)]+d^x[\vec{i}+(11)]-d^x[\vec{i}+(01)]\}/2$, where $d^x(\vec{i})$ and $d^y(\vec{i})$ represent the displacement of the atom at site $\vec{i}$ along x (horizontal) and y (vertical) directions, respectively. Intercell modes e_1, e_2, and e_3, correspond to dilatation, shear, and deviatoric long wavelength modes. Intracell modes s_x and s_y correspond to the normal coordinates of the zone boundary mode.

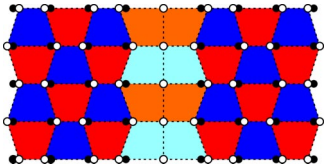

FIG. 2. (Color online) An example of the atomic displacement pattern on either side of an APB. Solid and open circles represent atomic positions for undistorted square lattice and distorted lattice, respectively. Red and blue (different gray scales) represent the positive and negative signs of the s_x mode defined for each plaquette.

modes $(\tilde{s}_x,\tilde{s}_y)$ always generate *intercell* modes $(\tilde{e}_1,\tilde{e}_2,\tilde{e}_3)$, which provides a microscopic origin to the phenomenological gradient energy term in continuum elasticity theory. Therefore, intercell modes are present inside an APB at which an intracell mode with tilde changes its sign. Similar arguments apply to a TB—the spatial variations of intercell modes always generate intracell modes inside a TB through their constraints—and lead to a similar solitary profile for TB and APB.[4,10] However, there exists a fundamental difference between intercell and intracell modes: In the $k\rightarrow 0$ limit, e_1, e_2, and e_3 are given as a first derivative of d_x and d_y, whereas in the $q\rightarrow 0$ limit, $\tilde{s}_x$ and $\tilde{s}_y$ are $2\tilde{d}_x$ and $2\tilde{d}_y$. Therefore, e_1, e_2, and e_3 are related by constraint equations, whereas $\tilde{s}_x$ and $\tilde{s}_y$ are not constrained by each other.

We consider the APB between the two ground states with $\tilde{s}_x(\vec{i})=\pm\sqrt{D/G_1}=\pm s_x^0$ (Fig. 2). On expanding Eq. (1) around the ground state and retaining leading order terms, we write the energy $E_{\mathrm{APB}}=E_{\mathrm{APB,OP}}+E_{\mathrm{APB,NOP}}$, where

$$E_{\mathrm{APB,NOP}}=\sum_{\vec{i},n=1,2,3}\frac{C_n}{2}\tilde{e}_n(\vec{i})^2+\sum_{\vec{i}}\frac{D'}{2}\tilde{s}_y(\vec{i})^2, \tag{2}$$

$$E_{\mathrm{APB,OP}}=\sum_{\vec{i}}\left\{-\frac{D}{2}\tilde{s}_x(\vec{i})^2+\frac{G_1}{4}\tilde{s}_x(\vec{i})^4\right\}, \tag{3}$$

and $D'=D(G_2/G_1-1)$. The energy E_{APB} has the identical form to that for a TB with e_3 as OP—a double-well potential for OP and harmonic potentials for non-OP. For both TB and APB problems, the non-OP energy terms mediate an anisotropic interaction between OPs through the constraints. The minimization of $E_{\mathrm{APB,NOP}}$ using Lagrange multipliers leads to $E^{\min}_{\mathrm{APB,NOP}}=\Sigma_{\vec{q}}\frac{1}{2}\tilde{s}_x(-\vec{q})\tilde{U}(\vec{q})\tilde{s}_x(\vec{q})$, where $\tilde{U}(\vec{q})$ has a q^2 leading order term with an anisotropic coefficient $\tilde{U}_2(\theta_q)=[(C_1+C_2+C_3)+(C_2-C_1-C_3)\cos 2\theta_q]/16$. When transformed into real space in 2D, the q^2 leading order term gives rise to a short range R^{-4} interaction between OP's $\tilde{s}_x$, in contrast to the long-range R^{-2} interaction between OP's e_3 for the TB case, where R is the distance between two sites.[11–13] Such different ranges of interactions are consistent with our understanding[7] of smoothness and roughness of TBs and APBs, that our simulations reproduce.

The physical origin of the long-range interaction between *intercell* modes and short-range interaction between *intracell* modes lies in the difference in the symmetry operations relating the two domains separated by a TB or APB. For a TB, the sign change in the OP corresponds to a change in orientation, which has no intrinsic length scale and thus gives rise to a long-range interaction. For an APB, the sign change in the OP signifies translation of the configuration by one atomic spacing, implying the presence of an intrinsic atomic length scale that is responsible for the fast decay of the interaction between OPs. These considerations apply to any 2D/3D lattice with monoatomic or multiatomic bases. We can also expect it to be valid for the rough and fluctuating stripes suggested in high-T_C cuprates, which are examples of magnetic APBs. Arguments similar to those in Ref. 14, related to the range of the interactions, explain the characteristic smoothness and roughness of TBs and APBs.

The full expression of the kernel $\tilde{U}(\vec{q})$ in $E^{\min}_{\mathrm{APB,NOP}}$ is given by

$$\tilde{U}(\vec{q})=[(C_1+C_3)/2]T_y(\vec{q})^2+(C_2/2)T_x(\vec{q})^2-\frac{(C_1+C_2-C_3)^2T_x(\vec{q})^2T_y(\vec{q})^2}{4D'+2(C_1+C_3)T_x(\vec{q})^2+2C_2T_y(\vec{q})^2}, \tag{4}$$

where $T_x(\vec{q})=\tan(q_x/2)$ and $T_y(\vec{q})=\tan(q_y/2)$. We choose similar parameter values for both APB and TB cases and use the Euler method[11,12,15] to relax the total energy associated with the lattice starting from random initial conditions. The simulation corresponds to a rapid quench to temperature $T=0$ and it shows differences in the formations of TBs and APBs in the course of the evolution. The results, e_3 for TB and $\tilde{s}_x$ for APB, on a 64×64 lattice with periodic boundary conditions are shown in Figs. 3 and 4, respectively, where the main panels show real space distributions and insets the k- or q-space distributions. Figures 3(a) and 4(a) correspond to early stages of the relaxation, whereas Figs. 3(b) and 4(b) reflect the OP distributions for late stages. Even at the early stage, the presence of the long-range correlation between the intercell OP along 45° and 135° can be identified in the main panel in Fig. 3(a), reminiscent of tweed structures in martensitic and other multiferroic materials. The k-space distribution plotted in the inset of Fig. 3(a) shows strong preference of $e_3(\vec{k})$ along 45° and 135° orientations. Such long-range correlation and anisotropy are absent for the phase of the intracell mode distortion, as shown in Fig. 4(a). The late stage of the relaxation depicted in Figs. 3(b) and 4(b) shows characteristic smooth TBs and rough APBs. The TB is metastable and cannot be removed by further relaxation, unless large amplitude noise is applied. In contrast, the APB in Fig. 4(b), which is a ring due to the periodic boundary condition, shrinks and disappears upon further relaxation. Although the solitary-wave profile of the smooth APB along a certain direction is a metastable state, the absence of a long-range interaction between the phase of intracell mode distortions prevents the relaxation of random initial configuration from reaching such metastable states. This indicates that lattice defects or boundary conditions are necessary to reach the metastable solitary-wave APB configuration in materials, and they influence the geometry of APBs.

To study functional electronic aspects associated with these TB and APB microstructures, we consider the modulation of electronic properties based on the following SSH electron-lattice coupling Hamiltonian

$$H_{\mathrm{SSH}}=\sum_{\vec{i},a=x,y}-t_0[1-\alpha(d^a_{\vec{i}+\hat{a}}-d^a_{\vec{i}})](c^\dagger_{\vec{i}}c_{\vec{i}+\hat{a}}+c^\dagger_{\vec{i}+\hat{a}}c_{\vec{i}}), \tag{5}$$

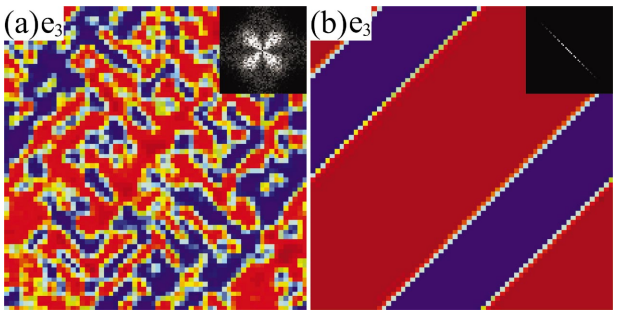

FIG. 3. (Color) $e_3(\vec{i})$ (main panels) and $|e_3(\vec{k})|$ (insets) obtained from simulation for TB: (a) early and (b) late stages of the lattice relaxation. Parameter values (see Ref. 8 for the definitions) are $A_1=A_2=B=4$, $A_3'=5$, and $F_3=50$. The center of the inset corresponds to $\vec{k}=0$ and the four corners $\vec{k}=(\pm\pi,\pm\pi)$. [Dark red: 0.32, dark blue: −0.32, white color in the inset: larger than 0.2 times the maximum of $|e_3(\vec{k})|$.]

where $c_{\vec{i}}^{\dagger}$ is the creation operator for an electron at $\vec{i}$. We use $d^x(\vec{i})$ and $d^y(\vec{i})$ obtained from our atomistic model as inputs to the SSH Hamiltonian.[16] For $t_0=1$, $\alpha=1$, and the TB and APB results shown in Figs. 3(b) and 4(b), we find all energy levels and eigenstates numerically, and calculate the local density of state (DOS) at each site and the distributions of local DOS and charge density for chosen Fermi energies (E_F), as shown in Figs. 5–7.

The blue curve in the inset of Fig. 5(a) represents the local DOS within the domain of Fig. 3(b), close to the bulk DOS for the homogeneous phase. The energy difference between the two peaks is proportional to $\alpha|e_3|$. Within the TB, $|e_3|$ is small and therefore the local DOS spectral weight moves toward $E=0$, as shown with a red curve. This local shift of the DOS weight can be measured using direct local probes, such as STM.[1,17] For the E_F shown in this inset, the local DOS is smaller inside the TB than inside the domain, and the main panel of Fig. 5(a) shows the real space distribution of local DOS at this E_F. The oscillation of local DOS within the domain is related to Friedel oscillations. The charge density, which is the area in the local DOS below E_F, is a constant (0.5) if $E_F=0$. If $E_F<0$, more electrons are depleted from the TB than the domain, as shown in Fig. 5(b). The charge density also has a Friedel oscillation, though not clearly visible in Fig. 5(b). The feedback from electron to lattice ne-

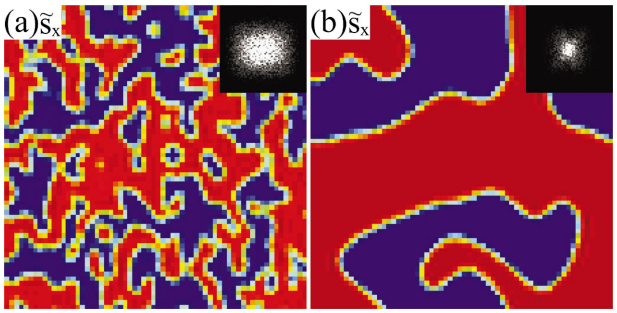

FIG. 4. (Color) $\tilde{s}_x(\vec{i})$ (main panels) and $|\tilde{s}_x(\vec{q})|$ (insets) distributions obtained from simulations for APB: (a) early and (b) late stage of the lattice relaxation. Parameter values are $C_1=C_2=C_3=D'=4$, $D=5$, and $G_1=50$.

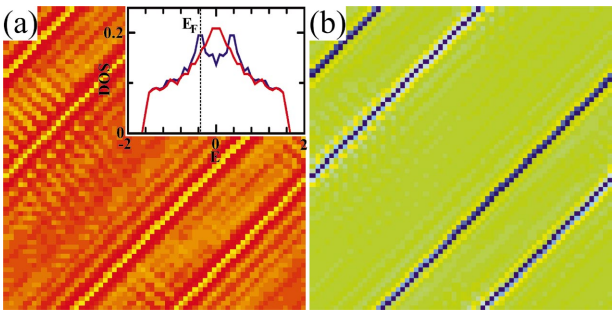

FIG. 5. (Color) Electronic properties calculated for the lattice distortion in Fig. 3(b). (a) Inset: local DOS within the domain (blue curve) and TB (red curve); main panel: spatial distribution of local DOS at E_F. (b) Corresponding charge density distribution (dark blue: 0.36, green: 0.39).

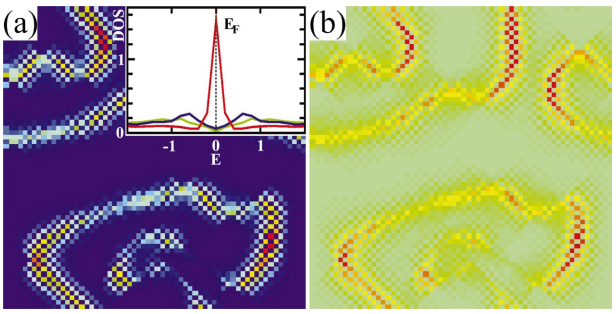

FIG. 6. (Color) Electronic properties calculated for the lattice distortion in Fig. 4(b). (a) Inset: local DOS within the domain (blue curve) and APB (red and green curves); main panel: spatial distribution of local DOS at $E_F=0$ (dark blue: 0, dark red: 2). (b) Spatial charge density distribution for $E_F=0.1$ (green: 0.52, dark red: 0.72).

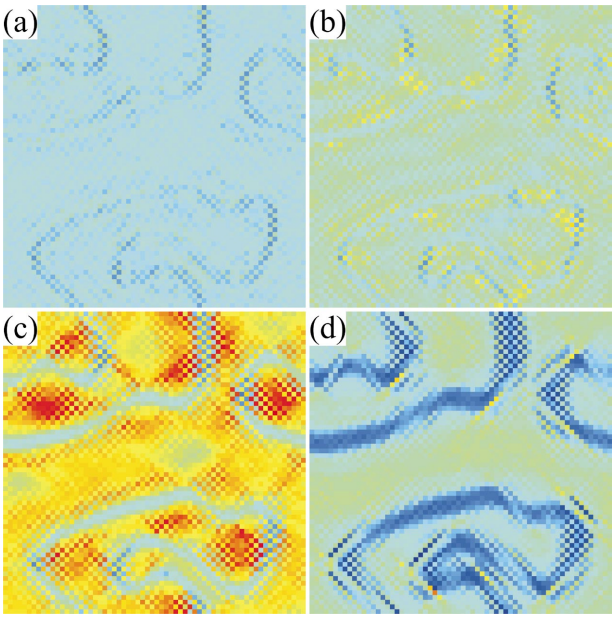

FIG. 7. (Color) Local DOS calculated for the lattice distortion in Fig. 4(b) at various E_F values (a) −1.5, (b) −1.1, (c) −0.7, and (d) −0.3 (dark red: 0.35, dark blue: 0).

glected here may generate a similar Friedel oscillation of the lattice, although the effect for the case in Fig. 5 would be too small to be observed.

The inset of Fig. 6(a) shows the local DOS for the APB case. Within the domain, in spite of the (π,π)-type lattice distortion, each site has one closer and one further neighbor in the horizontal direction (Fig. 2). Due to the symmetry between left and right inside the domain, the electronic properties are still homogeneous, but such a distortion pattern results in a V-shaped local DOS with zero DOS at $E=0$, plotted as a blue curve in the inset of Fig. 6(a) (the small finite value of local DOS at $E=0$ is due to the finite energy bin size). Near the *vertical* APB, the symmetry between left and right is broken, which brings out the effect of (π,π) type lattice distortions in the electronic properties, as shown in the main panels of Fig. 6. For example, along sites at the center of the vertical APB shown in Fig. 2, the neighboring sites in the horizontal direction are alternately closer or further apart. The red line in the inset of Fig. 6(a) represents the local DOS for the sites with two further neighbors within the center of the APB. This has a peak near $E=0$. The green line represents the local DOS at sites with two closer neighbors, right next to the sites for the red curve along the vertical direction. The difference between the red and green curves emphasizes the difference that occurs in density of states due to atomic-scale changes in microstructure along an APB. Such atomistically sharp changes at structural interfaces have been observed in CMR manganites with STM (Renner *et al.*[1]). The local DOS at $E_F=0$ is zero within the domain and finite only around the APB with a (π,π) component modulation, as depicted in the main panel of Fig. 6(a). [We note that the (π,π) modulation is weaker near the horizontal part of the APB.] This means that the electronic states created by the APB dominate the low energy properties of the whole system, e.g., conductivity or specific heat. The charge density for E_F slightly higher than zero is plotted in Fig. 6(b). Checkerboard-type modulations of electronic properties around APBs, reflecting the electronic states coupled to the (π,π)-type lattice distortions, demonstrate that STM studies of TB and APB can be used to reveal underlying electronic properties of materials (usually hidden in a homogeneous phase), similar to the way that single impurity atoms have been used to reveal superconducting properties in high-T_C cuprates. Results for different values of E_F are displayed in Fig. 7. Local DOS modulations, particularly the checkerboard-type modulations, tend to reach even further into the domain than the elastic texture itself. We also note that the checkerboard type modulations with a wave vector (π,π) are present at any E_F, in contrast to Friedel oscillations for TBs which change wave vectors with E_F. Though specific details found here would depend on the types of APB, it is still expected that the wave vectors of electronic modulations near different types of APB are related to the wave vector of underlying lattice distortions irrespective of E_F.

Although the orbital states and type of electron-lattice coupling in CMR manganites are different from the simple model presented here, our results suggest that simple APBs from double-well type potentials, such as Eq. (3), may give rise to electronic heterogeneities, but not undistorted metallic regions with uniform charge densities near APBs. An energy landscape with a local minimum at the undistorted state, such as the one considered in Ref. 18, would be more likely to nucleate metallic domains at APBs, and create percolating conducting paths in CMR manganites.

In summary, we have shown that in functional materials with strong electron lattice coupling, the electronic properties are distinctly modified near elastic textures such as TBs and APBs, which can be directly measured by STM. The results also show that the heterogeneities of electron local DOS are not confined within TBs and APBs, but can propagate into domains in the form of Friedel oscillations for TBs and with the wave vector related to short wave length lattice distortions for APBs.

This work was supported by the US DOE.

*Present address: Advanced Photon Source, Argonne National Laboratory, Argonne, IL 60439. Email: kenahn@aps.anl.gov

[1] M. Uehara *et al.*, Nature (London) **399**, 560 (1999); Ch. Renner *et al.*, *ibid.* **416**, 518 (2002); M. Fäth *et al.*, Science **285**, 1540 (1999); L. Zhang *et al.*, *ibid.* **298**, 805 (2002).

[2] N. Fukumoto *et al.*, Phys. Rev. B **60**, 12 963 (1999).

[3] A. M. Abakumov *et al.*, Phase Transitions **71**, 143 (2000).

[4] W. Cao *et al.*, Phys. Rev. B **64**, 024106 (2001); W. Cao and G. R. Barsch, *ibid.* **41**, 4334 (1990).

[5] X. Ren and K. Otsuka, MRS Bull. **27**, 115 (2002).

[6] Y.-A. Soh *et al.*, Phys. Rev. B **63**, 020402(R) (2000); Y.-A. Soh *et al.*, J. Appl. Phys. **91**, 7742 (2002).

[7] See, e.g., J. R. Barkley *et al.*,J. Appl. Phys. **44**, 938 (1973); V. A. Meleshina *et al.*, Sov. Phys. Crystallogr. **18**, 764 (1974); I. Rychetsky *et al.*, J. Phys.: Condens. Matter **5**, 1455 (1993).

[8] K. H. Ahn *et al.*, Phys. Rev. B **68**, 092101 (2003).

[9] The lattice with s_x or s_y mode distortions, which are Brillouin zone edge modes, is usually characterized as antiferroelasticity. The specific instability shown here can be originated from, for example, the softening of the central force potential between the nearest-neighbor atoms.

[10] G. R. Barsch *et al.*,Phys. Rev. Lett. **53**, 1069 (1984).

[11] S. R. Shenoy *et al.*, Phys. Rev. B **60**, R12 537 (1999).

[12] T. Lookman *et al.*, Phys. Rev. B **67**, 024114 (2003).

[13] In 3D, the long-range interaction due to strain $\sim R^{-3}$.

[14] Chapter 28 in S.-K. Ma, *Statistical Mechanics* (World Scientific, Philadelphia, 1985).

[15] We use relaxation type dynamics for OPs, s_x for APB, and e_3 for TB, as described by equations similar to Eq. (3) in Ref. 11, e.g., $ds_x(\vec{i})/dt=-\delta[E_{\mathrm{APB,OP}}+E^{\mathrm{min}}_{\mathrm{APB,NOP}}]/\delta s_x(\vec{i})$. The initial OP values are chosen randomly, e.g., between $-0.75\ s_x^0$ and $0.75\ s_x^0$. The scaled time step of the relaxation is chosen as $\Delta t=5\times10^{-4}$. Figures 3(a) and 4(a) are the configurations at $t=2000\ \Delta t$, and Figs. 3(b) and 4(b) at $t=40000\ \Delta t$.

[16] Thermal vibration of atoms and long range Coulomb interaction neglected here would broaden local DOS features and reduce the amplitude of the charge density modulation, respectively.

[17] S. H. Pan *et al.*, Nature (London) **413**, 282 (2001).

[18] K. H. Ahn *et al.*, Nature (London) **428**, 401 (2004).